This is a preprint, the final version is subject to change, of the American Mineralogist (MSA)
Cite as Authors (Year) Title. American Mineralogist, in press.
DOI: https://doi.org/10.2138/am-2020-7219

Revision 1

Orthovanadate wakefieldite-(Ce) in symplectites replacing vanadium-bearing omphacite in the ultra-oxidized manganese deposit of Praborna (Aosta Valley, Western Italian Alps)

Simone Tumiati[a,*], Marco Merlini[a], Gaston Godard[b], Michael Hanfland[c], Patrizia Fumagalli[a]

[a] Dipartimento di Scienze della Terra, Università degli Studi di Milano, Via Botticelli 23, 20133 Milano, Italy; *corresponding author: simone.tumiati@unimi.it

[b] Université de Paris, Institut de Physique du Globe de Paris, CNRS, F-75005 Paris, France

[c] ESRF, European Synchrotron Radiation Facility, 6 rue Jules Horowitz, 38043 Grenoble Cedex, France

Abstract

Because of their unique structure and properties, rare-earth (*REE*) orthovanadates are extensively employed since decades in advanced ceramics, in particular in the laser industry in replacement of Nd:YAG. Ca-bearing rare-earth orthovanadate with empirical formula $(Ce_{0.279}\,Ca_{0.271}\,Y_{0.267}\,Gd_{0.057}\,Nd_{0.055}\,Dy_{0.032}\,Sm_{0.027}\,La_{0.020}\,Th_{0.027}\,Sr_{0.002})\,(V^{5+}_{0.908}\,Cr^{3+}_{0.067}\,Fe^{3+}_{0.017}\,As^{5+}_{0.005})\,O_4 \bullet n\,H_2O$ has been found in metacherts from Praborna (Italian Alps), as micrometer-sized euhedral crystals in clinopyroxene + plagioclase symplectites replacing eclogite-facies vanadium-bearing omphacite ($Aegirine_{55–48}Jadeite_{42–33}Diopside_{10–8}$ with $V_2O_3 \leq 1.39$ wt%). We applied synchrotron radiation single crystal micro-diffraction technique, recently optimized at ID09A beamline (ESRF, France), to determine the crystal structure of this mineral. It is tetragonal and isostructural with zircon, with $a = 7.2233(12)$ Å, $c = 6.3949(18)$ Å, $V = 333.66(13)$ Å^3, $Z = 4$, spatial group $I4_1/amd$ and it has been therefore identified as Ca- and Y-bearing wakefieldite-(Ce) (ideally $CeV^{5+}O_4$). Cell parameters are in agreement with those of synthetic $Ce_{0.7}Ca_{0.3}VO_4$. Raman spectra of the studied wakefieldite-(Ce) are comparable with natural and synthetic wakefieldite-(Ce) spectra and revealed the presence of OH groups and/or water of hydration, which is also suggested by the low totals in microprobe analyses. Mass balance indicates that wakefieldite-(Ce) is a by-product of the omphacite breakdown; omphacite and Mn-rich epidote, a minor reactant, provided vanadium and *REE* respectively. Petrological observation and thermodynamic modeling suggest that the mineral, coexisting with hematite, Mn-rich epidote and braunite, formed during retrogression to greenschist-facies conditions at ultra-oxidized conditions ($\Delta FMQ \geq +16$ log units), which are often observed in Mn-oxide ores. Wakefieldite is an effective scavenger of *REE* in oxidized geological environments at *P–T* conditions that range from sedimentary to medium-grade metamorphic settings, even where the *REE* bulk concentration is negligible. Its rarity reflects both the overall low abundance of

vanadium and the scarcely recorded ultra-oxidized conditions in metamorphic rock systems, where *REE* phosphates (i.e., monazite, xenotime) are commonly found instead.

Keywords: vanadate, wakefieldite, manganese, Alps

Introduction

Rare-earth (*REE*) orthovanadates are known in materials science because of their uncommon properties. Neodymium-doped YVO_4, $GdVO_4$ and $LuVO_4$ are very efficient laser host crystal (vanadate lasers: e.g., O'Connor 1966). $CeVO_4$ is a semiconductor, showing outstanding redox and optical properties, which is used as a biological safeguard against inflammation and radiation injury because of its oxidation resistance, and could serve as potential solar-driven photocatalyst and anticancer agent (Chang et al. 2019, and references therein). Surface V^{5+} species are known to closely interact with Ce^{4+}, which unlike other lanthanides can be stable in water (e.g., Yu and O'Keefe 2006), reducing it to Ce^{3+}-forming insoluble $Ce^{3+}V^{5+}O_4$ (Martínez-Huerta et al. 2004). Moreover, Ca-bearing $CeVO_4$ could incorporate even some Ce^{4+} in a stable solid form (Petit et al. 2011).

Wakefieldite, a natural *REE* orthovanadate of the xenotime group with ideal formula $REEV^{5+}O_4$ and zircon-type structure, is rare but known to occur preferentially in highly-oxidized rocks, in particular in Mn-oxide ores (Baudracco-Gritti et al. 1987; Cadoni et al. 2011; Gröbner et al. 2011; Moriyama et al. 2011; Walter et al. 2018). Wakefieldite was discovered first as wakefieldite-(Y) in an hematite- and goethite-bearing pegmatite at Wakefield Lake, Quebec (Canada) (Miles et al. 1971), followed by wakefieldite-(Ce) found in the oxidation zone of silicified limestones at Kusu (Zaire) and known formerly as kusuïte (Deliens and Piret 1977), wakefieldite-(La) from the manganese and iron Glücksstern Mine associated with hausmannite $Mn^{2+}Mn^{3+}{}_2O4$ (Thuringia, Germany) (Witzke et al. 2008) and wakefieldite-(Nd) in the Arase stratiform hematite-bearing ferromanganese deposit (Kochi prefecture, Japan) (Moriyama et al. 2011). Wakefieldite-(La), along with a series of vanadium- and *REE*-bearing minerals, has been reported also in low-grade obducted manganese-rich radiolarites covering the Ligurian ophiolites (Supplementary Table 1), which have been suggested as representative of the protolith of the Praborna eclogite-facies metacherts (Tumiati et al. 2010).

In this paper, we study a new wakefieldite occurrence that we observed in some ultra-oxidized Mn-rich rocks from Praborna (Italian Western Alps). After a chemical and crystallographic characterization of the mineral, we present a detailed petrological study and a thermodynamic

modeling, in order to deduce the formation conditions of this mineral.

Geological setting

The Praborna manganese ore (Saint-Marcel valley, Italy; Fig. 1), hosted in metaophiolites belonging to the Zermatt-Saas unit of the Western Italian Alps, has been interpreted as an hydrothermal Mn-oxide deposit embedded in cherts covering the Jurassic oceanic lithosphere of the Alpine Tethys, subducted to eclogite-facies conditions during the Alpine orogeny (e.g., Tumiati et al. 2010). Hydrothermalism is likely constrained to Late Jurassic during an advanced stage of the opening of the Alpine Tethys, as demonstrated in the adjoining Aouliletta unit (Toffolo et al. 2017). High-pressure metamorphic peak conditions of P = 2.1 GPa and T = 550 °C are recorded in the nearby meta-ophiolite of the Saint-Marcel valley (Martin et al. 2008), and are assumed to also represent the eclogite-facies peak conditions of Praborna metacherts (Tumiati et al. 2015). These P–T estimates are consistent with metamorphic peak conditions at T = 540 ± 20°C and P = 2.3 ± 0.1 GPa reported by Angiboust et al. (2009) for Zermatt-Saas ophiolites.

The Praborna Mn-deposit displays a continuous change in mineralogy from the basal levels in contact with glaucophanite, partly retrogressed to greenschist facies, towards the upper levels in contact with Mn-poor metasediments, mostly due to an oxygen fugacity gradient between the strongly oxidized basal levels and the less oxidized upper levels. The basal levels (ΔFMQ > +12.5; Tumiati et al. 2015) contain braunite (the ore mineral), piemontite and purple Mn^{3+}-bearing omphacite (up to 64 mol% jadeite: Tumiati et al. 2015). The upper levels are characterized by the assemblage garnet (spessartine–grossular ± calderite) + aegirine-rich clinopyroxene ± pyroxmangite, the high-pressure polymorph of rhodonite $MnSiO_3$ (Fig. 1). Because of the strongly oxidized conditions, sulfides are not stable in any Mn-rich level. Therefore, chalcophile elements enter the structures of silicates and oxides, in particular ardennite-(As) (hydrous silico-arsenate of aluminum and manganese), hydroxycalciorouméite (calcium antimonate; cf. also Brugger et al. 1997), Sb-rich pyrophanite ($MnTiO_3$) and rutile, and As-bearing apatite (Tumiati et al. 2015). They also enter braunite, which contains 2500 µg/g (i.e., ppm) Co, 2000 µg/g Cu and 1100 µg/g Zn, and piemontite, with 450 µg/g As, 450 µg/g Ni and 360 µg/g Zn (Tumiati et al. 2010).

At Praborna, several minerals rich in rare earths have been described. Veins crosscutting the basal levels contain *REE*-rich piemontite, with maximum *REE* = 0.24 atoms per formula unit (a.p.f.u.) on the basis of 12.5 equivalent oxygens and Ce/La = 2.36 (Tumiati et al. 2015). In the upper levels, manganiandrosite-(Ce) occurs instead of piemontite as an accessory phase (Cenki-Tok et al. 2006).

It is characterized by Ce/La = 8.53 and contains 1800 μg/g Ni, 1680 μg/g Zn, 1400 μg/g Cu and 1400 μg/g Co (Tumiati et al. 2010).

Between the basal braunite-piemontite-rich level and the upper garnet-rich levels, a 10-cm-sized Mn-poor emerald-green layer (Fig. 1; cf. level 3 of Tumiati et al. 2010, sample 18/03) contains vanadium-bearing, aegirine-rich omphacite together with quartz. Accessory phases are Cr-rich phengite, Mn-rich epidotes bearing *REE* and Cr, Cr-bearing hematite and braunite, As-bearing apatite, native gold and (*REE*, Ca)-vanadates, which are the subject of this study.

Materials and methods

Two polished thin sections have been selected for this study: 1) sample 26/03, and 2) sample SM96-2. Both samples were collected from the emerald-green layer between the basal and the upper levels and are coincident with sample 18/03, for which Tumiati et al. (2010) provided the bulk-rock major- and trace-element geochemistry, as well as the petrographic description of the rock. Mineral abbreviations are from Whitney and Evans (2010) with the addition of Nt for natalyite and Nam for namansilite.

Electron microscopy and electron microprobe analyses

Scanning-electron microscopy, X-ray element mapping and quantitative analyses of minerals were performed using a JEOL 8200 wavelength-dispersive (WDS) electron microprobe (EMP). Point analyses were carried out at 15-kV accelerating potential, 15-nA sample current and 1-μm beam diameter. Standards used were: omphacite (Na), wollastonite (Si), anorthite (Ca, Al), fayalite (Fe), olivine (Mg), orthoclase (K), rhodonite (Mn), ilmenite (Ti), yttrium phosphate (Y, P), Pr phosphate (Pr), Nd phosphate (Nd), La phosphate (La), Sm phosphate (Sm), Ce phosphate (Ce), Dy phosphate (Dy), Gd phosphate (Gd), Eu phosphate (Eu), uraninite (U), niccolite (As), pure Cr (Cr), pure vanadium (V), hornblende (F) and scapolite (Cl). A counting time of 30 sec was applied for all elements. The Fe^{3+}/Fe_{TOT} and Mn^{3+}/Mn_{TOT} ratio in minerals reported in Table 1, 2 and 3 have been calculated by stoichiometry and charge balance, following the procedure outlined in Tumiati et al. (2015). V^{5+} is assumed to occur in wakefieldite, and V^{3+} in the other minerals.

Synchrotron single crystal X-ray microdiffraction

Structural determination of the (*REE*, Ca)-vanadate has been performed employing the newly optimized diffraction setup at ID09A ESRF synchrotron beamline (Grenoble, France). The setup is particularly suited for single crystal micro-diffraction at extreme conditions (Dubrovinsky et al.

2010; Merlini et al. 2012). It consists of a highly mechanical stable ω-goniometer, with rotation axis perpendicular to the monochromatic X-ray beam. The source is a 19-period undulator, which provides a high brilliance beam with an approximate section of 100×100 μm^2 on the optical components, constituted by a 1 m length mirror (for vertical focusing and high-harmonics cleanup) and a Laue-transmission (111) Si monochromator, for horizontal focusing. The beam section on the sample can then be easily tuned from a few μm^2 to 60×160 μm^2 depending on the purpose. The beamline design assures a minor divergence, and a quasi-parallel beam on the sample and detector. This feature is essential in order to reduce instrumental diffraction peak broadening. Together with newly upgraded 2D X-ray detector (Mar555 flat panel detector), with zero point-spread function, this feature assures not only the maximum resolution currently achievable by 2D detectors and parallel beam, but also the possibility to fully separate geometrically close diffraction peaks during intensity integration procedure. This characteristic is highly required in complex crystallographic experiments, in order to treat each crystalline domain as a single crystal in polycrystalline samples. The structure determination of this vanadate is a highly demanding issue, since it forms very small crystals within a matrix composed mainly by pyroxenes and feldspars (see below). Isolation of single crystals of average size 4×4×4 μm^3 is in fact very difficult. The possibility to mount a petrographic thin section directly on the X-ray goniometer allows accurate structure determination on previously identified micro-crystals by optical methods and microprobe analysis. The diffraction experiments have been performed with a monochromatic beam (λ = 0.414 Å), with a section of 10×10 μm^2 on the sample, in order to have the target fully immersed in X-ray beam during data collection. A closely occurring hematite crystal (Fig. 3 BSE) has been used in order to align properly the target in the center of goniometer by X-ray absorption scans at different ω-angles. Then, by optical methods, the wakefieldite crystal section (Fig. 3) was positioned in the center of X-ray beam. X-Ray data have been collected with a 60° ω-scan, with a step-size of 0.5°, integrated over an exposure of 1 sec.

The 2D diffraction data from Mar555 detector have been analyzed with the Crysalis software (Oxford Diffraction, 2008, Crysalis RED, version 1.171.32.39) and successively treated with Superflip and Jana2006 software (Palatinus and Chapuis 2007; Petříček et al. 2014). No absorption correction has been applied, since absorption from the glass of the thin section is negligible at 30 keV and however is implicitly taken into account in empirical rescaling of frames. No diffraction volume correction was also needed, since all the crystal was immersed in the X-ray beam during the ω-rotation scans. Finally, no beam intensity variation was considered, since within the 15 minutes data collection time the primary synchrotron beam intensity is constant.

Micro-Raman spectroscopy

The same crystal characterized by electron microprobe and by single crystal synchrotron X-ray diffraction was investigated with a Horiba LabRam HR Evolution micro-Raman spectrometer equipped with a green solid-state laser (532 nm) focused through a 100× objective, giving a spatial resolution of approximately 1 μm. The micro-Raman system was set with 600 lines/mm grating; the spectrum was collected with a final laser power of about 30 mW at the sample surface measured through a handheld power meter. Spectra were calibrated using the 520.7 cm^{-1} line of a silicon wafer.

Thermodynamic modeling

The thermodynamic modeling of petrological reactions involving wakefieldite is hampered by the lack of many thermodynamic properties and of solution models concerning, among others, the $NaV^{3+}Si_2O_6$ (natalyite) end-member in omphacite and the *REE* end-members (manganiandrosite, dissakisite, allanite) in epidote. Nevertheless, the *P–T–f*O_2 stability of vanadium oxides ($V^{2+}O$, $V^{3+}{}_2O_3$, $V^{4+}O_2$, $V^{5+}{}_2O_5$) can be somewhat indicative of the stability of wakefieldite, whose formula is $REE_2O_3 \bullet V^{5+}{}_2O_5$. Therefore, we calculated univariant equilibria between the different vanadium oxides using the Gibbs free energies of formation, the molar volumes and the entropies in the standard state, and the heat capacity parameters reported by Weast (1984). The thermal expansion and bulk modulus parameters were borrowed from the iron oxide hematite (Supplementary Table 2). We verified that the used parameters for vanadium oxides well reproduce published *p*O_2–*T* phase diagrams calculated at room pressure using the commercial software FactSage (Kim et al. 2012). In addition, in order to constrain indirectly the conditions of formation of wakefieldite, we calculated a *P–T* isochemical phase diagram (i.e., *P–T* pseudosection) in the system Na_2O–CaO–FeO–MgO–MnO–Al_2O_3–SiO_2–H_2O–O_2 using the local domain composition of the host clinopyroxene + plagioclase symplectite (obtained by image analysis and mass balance calculations), as the growth of wakefieldite and of symplectite-forming minerals occurred at apparent textural equilibrium. Thermodynamic calculations were performed with the Perple_X package (http://www.perplex.ethz.ch; Connolly 2005), using the thermodynamic database of Holland and Powell (1998) revised in 2004 (hp04ver.dat) and enlarged with manganese oxides and end-member piemontite (Tumiati et al., 2015; Supplementary Table 2). The following solid solution models were used: i) Gt(HP) for spessartine-grossular garnet (Holland and Powell, 1998); ii) Omph(HP) for aegirine–jadeite–diopside–Ca-Tschermak–hedenbergite clinopyroxene (Holland and Powell 1996) iii) Pl(I1,HP) for plagioclase (Holland and Powell, 1998). Because thermodynamic models are not available for the solid solution between piemontite [$Ca_2Al_2Mn^{3+}Si_3O_{12}(OH)$] and

204 epidote *sensu stricto* [$Ca_2Al_2Fe^{3+}Si_3O_{12}(OH)$], ideal mixing has been assumed for Mn-bearing
205 epidote.

206 **Results**

207 **Petrography and mineral chemistry**

208 *Peak assemblage*

209 The eclogite-facies peak assemblage consists of quartz, omphacite, epidote and various accessory
210 minerals.

211 Emerald-green omphacite is rich in aegirine (Aeg) and contains vanadium, likely in the form of the
212 natalyite end-member (Nt: $NaV^{3+}Si_2O_6$), as suggested by the strong positive correlation between Na
213 and V in microprobe analyses (Supplementary Fig. 1a). The highest vanadium contents in
214 omphacite were measured in sample 26/03 (Table 1), characterized by a bright emerald-green color.
215 There, vanadium displays a patchy zoning (Fig. 2), with a maximum V_2O_3 content of 1.39 wt% (4
216 mol% Nt), and an average composition $Aeg_{55}Jd_{33}Di_8Nt_2Hd_1$ for the omphacite cores . In sample
217 SM96-2, the average composition of the omphacite cores is $Aeg_{48}Jd_{42}Di_{10}Nt_0Hd_0$, showing a lower
218 vanadium content (≤0.07 wt% V_2O_3) (Table 1).

219 In both samples, epidote is rich in Mn, close to piemontite. The core of the crystals commonly
220 shows *REE*- and Mg-rich patches, with Σ*REE* = 0.43 a.p.f.u., Ce/Σ*REE* = 0.59 and traces of V (up
221 to 0.81 wt% V_2O_3), giving the following representative composition ($Ca_{1.289}\,Sr_{0.069}\,Ce_{0.253}\,La_{0.133}$
222 $Nd_{0.029}\,Pr_{0.016}$) ($Al_{1.990}\,Fe^{3+}_{0.526}\,Mn^{3+}_{0.311}\,Mg_{0.177}\,As_{0.002}\,V_{0.001}$) $Si_{3.022}\,O_{12}\,(OH)$. This local
223 composition reflects an enrichment in the dissakisite end-member [(Ca*REE*)(Al_2Mg)Si_3O_{12}(OH); cf.
224 (Tumiati et al. 2005; Lavina et al. 2006)] at the metamorphic peak conditions. Nevertheless, the
225 average composition of the epidote cores remains negligible in V and low in *REE*, with an average
226 formula of ($Ca_{1.903}\,Sr_{0.029}\,Ce_{0.003}\,Nd_{0.002}\,Pr_{0.001}$) ($Al_{2.055}\,Fe^{3+}_{0.501}\,Mn^{3+}_{0.343}\,Mn^{2+}_{0.102}\,Cr^{3+}_{0.015}\,Mg_{0.006}$
227 $Ti_{0.003}$) $Si_{3.037}\,O_{12}\,(OH)$ (sample SM96-2; Table 2).

228 Cr-bearing phengite (or "mariposite") also displays a light emerald-green color, and its composition
229 is: ($K_{0.97}\,Na_{0.02}$) ($Al_{1.31}\,Mg_{0.49}\,Fe_{0.14}\,Cr_{0.07}\,Mn_{0.03}\,Ti_{0.01}$) ($Si_{3.54}\,Al_{0.46}$) $O_{10}\,(OH)_2$ (sample 26/03).
230 Phengite is zoned, showing an enrichment in Cr up to 0.36 a.p.f.u. (on the basis of 11 equivalent
231 oxygens; 6.38 wt% Cr_2O_3) towards the rim in textural equilibrium with retrograde minerals. Other
232 accessory minerals are Cr-bearing hematite (≤3.51 wt% Cr_2O_3), rutile (≤0.82 wt% Cr_2O_3) and
233 braunite (≤0.52 wt% Cr_2O_3).

234

235 *Retrograde assemblage*

236 Omphacite crystals are always surrounded by symplectites of plagioclase ($Ab_{98.6}$; Table 2) and
237 clinopyroxene (Fig. 2). This retrograde clinopyroxene, depleted in jadeite and in vanadium relative

to omphacite, has an average composition of $Aeg_{50}Di_{42}Jd_6Hd_1Kos_1Jhn_1$ in sample SM96-2 and $Di_{64}Aeg_{21}Jd_{13}Hd_3Jhn_1$ in sample 26/03 ("sympl. Cpx" in Table 1). Image analysis indicates that the symplectites consist of about 40 vol% clinopyroxene and 60 vol% plagioclase, with minor hematite, rutile and (*REE*, Ca)-vanadates (Figs. 2, 3).

Micrometer-sized vanadates have been found in these symplectites after omphacite as honey-yellow tiny euhedral crystals (Supplementary Fig. 2) in both samples 26/03 (Figs. 2) and SM96-2 (Fig. 3 and 4). This study is focused on the largest 10-µm-sized vanadate crystal found (sample SM96-2; Figs. 3a and 4, and Supplementary Fig. 2), which has been identified as wakefieldite on the basis of X-ray diffraction data (Table 3) and Raman spectroscopy (Fig. 5). This crystal as well as the associated hematite contain tiny inclusions of plagioclase (Fig. 4 BSE), which testifies that these minerals also formed in the symplectites after omphacite. Element X-ray maps and microprobe analyses show that it is chemically zoned (Fig. 4; Table 4), showing parts richer in Ce [Ce/(Σ*REE*+Y) up to 0.56; i.e., wakefieldite-(Ce)] and some others in Y [Y/(Σ*REE*+Y) up to 0.66; i.e., wakefieldite-(Y)]. The negative correlation between Y (+Dy) and Ce (+La+Ca+Nd+Sm) reflects the main substitution in the analyzed wakefieldite (Supplementary Fig. 1b). The composition of the investigated wakefieldite is rather complex, bearing up to 0.33 a.p.f.u. of Ca and minor Cr, Th and Fe (Table 4). The low totals of microprobe analyses suggest the presence of H_2O. Minor contents of F (0.30 wt%) and Cl (0.03wt%) were also detected. Assuming a trivalent state for Ce and H_2O as water of hydration only, the empirical average formula of the observed wakefieldite, given on the basis of 4 oxygens, is $(Ce_{0.279}\,Ca_{0.271}\,Y_{0.267}\,Gd_{0.057}\,Nd_{0.055}\,Dy_{0.032}\,Sm_{0.027}\,La_{0.020}\,Th_{0.027}\,Sr_{0.002})\,(V^{5+}_{0.908}\,Cr^{3+}_{0.067}\,Fe^{3+}_{0.017}\,As^{5+}_{0.005})\,O_4 \bullet n\,H_2O$.

The rims of the epidote crystals, in textural equilibrium with the retrograde assemblage, are enriched in Cr relative to the core of the same crystals (≤12.40 wt% Cr_2O_3), which resulted from the $Al_{-1}Cr^{3+}_{+1}$ substitution towards the tawmawite end-member [$Ca_2Al_2Cr^{3+}Si_3O_{12}(OH)$], with sometimes a Cr enrichment up to true tawmawite $(Ca_{1.80}\,Sr_{0.10}\,Mn^{2+}_{0.13})\,(Al_{1.43}\,Fe^{3+}_{0.60}\,Cr^{3+}_{0.84}\,Mg_{0.02}\,Fe^{2+}_{0.03})\,Si_{2.99}\,O_{12}\,(OH)$. The average composition of epidote rim in sample SM96-2 is $(Ca_{1.899}\,Sr_{0.023})\,(Al_{1.807}\,Fe^{3+}_{0.745}\,Mn^{3+}_{0.315}\,Mn^{2+}_{0.119}\,Cr^{3+}_{0.046}\,Mg_{0.003})\,Si_{3.042}\,O_{12}\,(OH)$ (Table 2), showing an enrichment in Cr and Fe, and a marked depletion in *REE* compared to the average composition of the core (see above).

The primary phengite (see above) is zoned, showing an enrichment in Cr up to 0.36 a.p.f.u. (on the basis of 11 equivalent oxygens; 6.38 wt% Cr_2O_3) towards the rim in textural equilibrium with retrograde minerals, with an evolution towards Cr-bearing muscovite.

Finally, the interstices between the crystals of the early assemblage contain several accessories, such as calcite, Na–Ca amphibole (winchite–tremolite solid solution), As- and Sb-bearing titanite

(up to 7.88 wt% Sb_2O_3; 1.14 wt% As_2O_3), As-bearing apatite (≤10.67 wt% As_2O_5), and native gold grains up to 100 μm in size.

X-ray diffraction data and structure refinement

The structure of the studied phase has been refined on the largest 10-μm-sized crystal found in sample SM96-2 (Figs. 3 and 4). We observed, in the integrated diffraction peak table, the presence of several single crystal domains, which can be indexed with the low-albite triclinic unit cell (Harlow and Brown 1980). Four main albite single crystal domains, corresponding to plagioclase inclusions (Fig. 4), have been identified, and therefore removed from the peak table. The remaining peaks can be indexed with a tetragonal unit cell, with lattice parameters $a = b = 7.2233(12)$ Å; $c = 6.3949(18)$ Å; $\alpha = \beta = \gamma = 90°$. The systematic absences are compatible with a possible space group $I4_1/amd$, further confirmed by structure solution with charge flipping algorithm (Oszlányi and Sütő 2004). The derived structural model has been refined, assuming a mixed occupancy of Ce and Ca in the large cation site. The mineral is isostructural with zircon $ZrSiO_4$ (Binks 1926; Robinson et al. 1971) and, therefore, corresponds to the mineral wakefieldite. Crystal data and interatomic distances (Å) for refined *REE* orthovanadates with zircon structure are summarized in Table 3. The refined data of the measured wakefieldite are comparable in particular with those of the synthetic $Ce_{0.7}Ca_{0.3}VO_4$ investigated by Petit et al. (2011), which shows a Ca/*REE* ratio close to the wakefieldite investigated in this study.

The lattice parameters can be used to model the shape of crystals, using appropriate software (©KrystalShaper and ©Stereonet). The contours thus obtained for sections close to {1.18 0.92 0.90} in the presence of {111} faces are similar to those of the studied crystal (Fig. 4 Y–La–Ce; Supplementary Fig. 3).

Raman spectroscopy

Raman spectra of the studied wakefieldite are comparable with wakefieldite-(Ce) spectra available in the RRUFF database (ID: R060542 and R060176; Yellow Lake, British Columbia, Canada; cf. Howard et al., 1995) and synthetic zircon-type wakefieldite-(Ce), which is the stable form of $CeVO_4$ up to 5.3 GPa at room temperature (Panchal et al. 2011). A representative spectrum is shown in Figure 4. Compared to published spectra, the investigated sample displays broader peaks, suggesting a disordered state. The most intense peak is observed at 868 cm^{-1} and, according to Panchal et al. (2011), represents the symmetric-stretching internal mode $\nu_1(A_{1g})$ related to the intratetrahedral V–O bonds. The two asymmetric-stretching modes $\nu_3(E_g)$ and $\nu_3(B_{1g})$ have been observed at 814 and 791 cm^{-1}, respectively. Three bending modes of the VO_4 unit were observed at

258 cm^{-1} [$v_2(B_{2g})$], 367 cm^{-1} [$v_2(A_{1g})$] and 473 cm^{-1} [$v_4(B_{1g})$]. The external modes [$T(B_{1g})$] were observed at 132 cm^{-1} and 238 cm^{-1}. The broad band at about 720 cm^{-1}, although it is not predicted by *ab-initio* calculations for $CeVO_4$ and YVO_4 (Manjón et al. 2010; Panchal et al. 2011), has been described also in synthetic YVO_4, especially at relatively high pressures. It has been interpreted as a second-order mode following Manjón et al. (2010). The band at 915 cm^{-1} has been observed in calcium vanadates (Ryu et al. 2006; Sharma et al. 2018) and therefore it is interpreted to reflect the high calcium content in the analyzed wakefieldite. The intense broad band at 3618 cm^{-1}, along with those at 3470 cm^{-1} and 3530 cm^{-1}, can be assigned either to symmetric OH stretching vibrations of OH units and/or water of hydration (Frost et al. 2006).

Discussion

Identification of the studied mineral

The ascription of the mineral to tetragonal wakefieldite is confirmed by the structure refinement and Raman spectra. The empirical formula ($Ce_{0.279}\,Ca_{0.271}\,Y_{0.267}\,Gd_{0.057}\,Nd_{0.055}\,Dy_{0.032}\,Sm_{0.027}\,La_{0.020}\,Th_{0.027}\,Sr_{0.002}$) ($V^{5+}_{0.908}\,Cr^{3+}_{0.067}\,Fe^{3+}_{0.017}\,As^{5+}_{0.005}$) $O_4 \bullet n\,H_2O$] represents a solid solution of about 1/3 $Ce^{3+}V^{5+}O_4$ [wakefieldite-(Ce)] + 1/3 $Y^{3+}V^{5+}O_4$ [wakefieldite-(Y)] + 1/6 $Ca_2V_2O_7 \bullet n\,H_2O$ [pintadoite], this latter end-member being a poorly-characterized "grandfathered" mineral (Hess and Schaller 1914, Hess 1925). The formula above is consistent with the solid solution limit in $Ce_{1-x}Ca_xVO_4$ series at $x < 0.4125$ reported by Petit et al. (2011) at room temperature. Above $x = 0.4125$, the pyrovanadate $Ca_2V_2O_7$ should form (Petit et al. 2011), displaying triclinic structure $P1(2)$ (Sharma et al. 2018), which should correspond to anhydrous pintadoite. Actually, we found in sample 26/03 tiny crystals of *REE*-free Ca-vanadate with empirical formula ($Ca_{1.72}\,Sr_{0.14}$) ($V^{5+}_{1.84}\,Cr^{3+}_{0.36}$) O_7, on which we will give further details in a future paper. The presence of water of hydration and/or hydroxide ions OH^-, reflected by the low totals of microprobe analyses, has been confirmed by Raman spectroscopy. In this study, waiting for further data, we attribute H_2O to water of hydration only. As for wakefieldite-(Ce) and wakefieldite-(Y), the number of formula units in the tetragonal unit cell is four (i.e., $Z = 4$), so the calculated density of the crystal is 4.99 g/cm^3.

Petrogenesis of the wakefieldite-bearing symplectite

In the Praborna manganese deposit, wakefieldite occurs solely in the clinopyroxene + plagioclase symplectites that replace vanadium-bearing omphacite, suggesting that wakefieldite formed as a product of a retrograde reaction involving omphacite. In order to build up wakefieldite, in addition to vanadium provided by omphacite, a *REE*-bearing reacting phase is required. As the only *REE*-

bearing phase observed in our samples is epidote**,** we suggest that this mineral is one of the reactants involved in wakefieldite petrogenesis. This assumption is supported by the fact that the *REE* content in epidote, which is significant in the core of the crystals and decreases in the rim parts in textural equilibrium with symplectites to concentrations often below the electron microprobe detection limit (cf. Section Petrography and mineral chemistry; Table 2**)**.

Mass balance calculations, performed by the least-square method using the mineral compositions of sample SM96-2, yielded the following wakefieldite-forming reaction:

1.556 omphacite + 1.090 quartz + 0.144 epidote =
1 clinopyroxene + 0.879 plagioclase + 0.050 hematite + 0.001 wakefieldite + 0.087 O_2 + 1 *Subst* + 1 *R* (Eq. 1).

The stoichiometric coefficients, in mol, are normalized to +1 mol of produced clinopyroxene (see Godard, 2009, for the method and software), and the other phases appear as reactants or products, depending on whether the stoichiometric coefficient obtained is respectively negative or positive. Omphacite, quartz and epidote are the reacting eclogite-facies peak minerals (av. Omp in Table 1; epidote av. core in Table 2). Clinopyroxene (av. sympl Cpx in Table 1), plagioclase (Table 2), hematite (Table 2) and wakefieldite (average wakefieldite in Table 4) are the symplectite-forming minerals replacing primary omphacite during retrogression. The vector *Subst* ($Fe_{+0.199}\,Mn_{+0.059}\,Mg_{-0.258}$) is a linear combination of the independent $Fe_{+1}Mg_{-1}$ and $Mn_{+1}Mg_{-1}$ substitutions, which occur very generally during multivariant "continuous" reactions that involve Fe–Mn–Mg-bearing minerals; this vector here accounts for the Fe–Mn–Mg exchange during the reaction itself between eclogite-facies reactants and retrograde products. The vector *R* gives the residuals in the sense of the least-square method ($R = Si_{0.0000}\,Al_{-0.0000}\,Cr_{+0.0077}\,Ti_{-0.0000}\,Fe_{-0.0000}\,Mn_{-0.0000}\,Mg_{-0.0000}\,Ca_{-0.0000}\,Na_{+0.0000}\,K_{+0.0016}\,V_{-0.0003}\,REE_{-0.0004}\,O_{0.0000}$). Its coordinates are here very low, indicating that the proposed reaction is satisfactorily balanced and occurs in an almost closed system.

The above reaction (Eq. 1) can be expressed in volume amounts of the minerals involved, by weighting by their molar volumes, taken from the dataset of Holland & Powell (1998, upgraded version S62 of 2012) for the main minerals and from this study for wakefieldite:

1.507 omphacite + 0.379 quartz + 0.307 epidote =
1 clinopyroxene + 1.362 plagioclase + 0.023 hematite + 0.0004 wakefieldite (Eq. 2).

The proposed reaction (Eqs. 1 and 2) correctly accounts for the microstructures observed. The reactants, namely omphacite, quartz and epidote, belong to the eclogite-facies paragenesis, whereas the products make up the secondary symplectite, including the minor by-products hematite and wakefieldite (Figs. 3, 4). Omphacite is by far the main reactant (68.7 vol.% of all reactants), which explains why the symplectite has mainly developed at its expense. The estimated volume amounts of clinopyroxene and plagioclase among the products (41.9% and 57.1%, respectively: Eq. 2) are comparable to those in the symplectites (≈ 40% and ≈ 60%), estimated by image analysis. The amount of wakefieldite produced is limited by the availability of vanadium and rare earths in the reacting minerals; in Equation 2, it accounts for only 0.017 vol% of the produced solids, which is consistent with its very low abundance (Figs. 2, 3).

The reaction results in an increase in volume of the solids ($\Delta V/V_{TOT}$ = +0.088; Eq. 2), which is typical of a reaction related to a drop of pressure. In fact, the reaction can also be regarded as a variant of the omphacite breakdown, which is commonly observed during the retrogression of high-pressure rocks (e.g., Holland 1980):

1 jadeite (in omphacite) + 1 quartz = 1 albite (in plagioclase) (Eq. 3).

The balanced reaction shows in addition that V and *REE* entering wakefieldite are provided by omphacite and epidote, respectively. Considering the difference in vanadium oxidation state in omphacite and wakefieldite, the following simplified redox reactions can be proposed:

1 $V^{3+}{}_2O_3$ (in omphacite) + 1 REE_2O_3 (in epidote) + 2 Mn_2O_3 (in epidote) =
2 $REE_1V^{5+}{}_1O_4$ (wakefieldite) + 4 MnO (in clinopyroxene) (Eq. 4)

and

1 $V^{3+}{}_2O_3$ (in omphacite) + 1 REE_2O_3 (in epidote) + O_2 = 2 $REE_1V^{5+}{}_1O_4$ (wakefieldite) (Eq. 5)

depending on whether the oxygen fugacity is internally buffered (Eq. 4) or externally buffered (Eq. 5).

P–T–fO_2 conditions of formation

The overall composition of the reactants at the onset of a continuous multivariant reaction and that of the products at the end of the same reaction are ideally equal in a closed system. The composition of this theoretical reacting microdomain, which consists of the atoms that have moved from reactants to products during the reaction, can be used to build a *P-T* pseudosection (e.g., Godard,

2009). We considered the overall composition of the products of the reaction (Eq. 1) to calculate such a *P-T* pseudosection in the system Na_2O–CaO–FeO–MgO–MnO–Al_2O_3–SiO_2–H_2O–O_2 (Fig. 6), neglecting the minor components (V_2O_3, REE_2O_3, Cr_2O_3, K_2O) that corresponds to end-members and minerals that cannot be modeled, like wakefieldite, whose thermodynamic properties are unknown. In addition, we added to this bulk composition 10 mol% braunite and 10 mol% piemontite end-member, in order to emphasize the phase relations of manganese-rich minerals. The resulting *P-T* pseudosection ideally displays two multivariant fields corresponding to the stability fields of the reactants and the products, and the transition from one field to the other yields the *P-T* evolution during the reaction (black star to yellow star in Fig. 6 b).

Univariant curves for the reactions i) 2 VO_2 + 0.5 O_2 = V_2O_5 at log (fO_2/1 bar) = –5.5, and ii) 2 VO_2 + 3 Mn_2O_3 = V_2O_5 + 2 Mn_3O_4 are also considered (Fig. 6 b). Thermodynamic modeling shows that plagioclase + Jd-poor clinopyroxene are expected to replace, during retrogression, the omphacite formed at peak *P–T* conditions (black star in Fig. 6 a, b; Martin et al. 2008). At T = 550°C, omphacite is breaking down at P < 1.3 GPa. The jadeite content of 6–13 mol% measured in the clinopyroxene (Table 1) and the presence of hematite in the symplectite (Figs. 3, 4) suggests lower pressures of about 0.8 GPa under greenschist facies (yellow star in Fig. 6 b). Because of the uncertainties of retrograde temperature estimates, a more realistic wider field, taking into account also the stability field of $V^{5+}{}_2O_5$ in agreement with the occurrence of wakefieldite (REE_2O_3•$V^{5+}{}_2O_5$), is evidenced with a red field in Figure 6 b.

While omphacite contains traces of V^{3+}, wakefieldite contains V^{5+}, which means that vanadium was oxidized from V^{3+} to V^{5+} during wakefieldite formation (cf. Eqs. 4 and 5). Thermodynamic modeling shows that oxidation to V^{5+} is possible following a retrograde *P–T* path even without increasing the absolute oxygen fugacity. Actually, because of the positive slope of the univariant equilibria involving vanadium oxides in log (fO_2/1 bar) vs. (P, T) diagrams (Supplementary Figure 4), stability fields can be crossed by changing temperature, pressure or both. In particular, high pressures and temperatures tend to stabilize low oxidation states, whereas low pressures and temperatures promote high oxidation states, which is in agreement with natural observations.

Compared to the fayalite–magnetite–quartz (FMQ) fO_2 buffer, often taken as a reference for the redox state of rocks (cf. Tumiati and Malaspina 2019), the ΔFMQ (= $\log fO_2^{sample} - \log fO_2^{FMQ}$) value required for the stability of wakefieldite spans from +10 at 800°C to +18 at 400°C at ambient pressure, and is poorly dependent on pressure (Supplementary Figure 4). At greenschist-facies conditions, assuming for instance P = 0.8 GPa and T = 500°C, ΔFMQ must be greater than +16, which is in agreement with ΔFMQ > +12.7 suggested by Tumiati et al. (2015) for the Praborna ultra-oxidized manganese deposit.

In these strongly oxidized environments, wakefieldite is an effective scavenger able to incorporate and concentrate large amounts of *REE* (in particular Ce^{4+} from aqueous fluids due to its reduction to Ce^{3+}; cf. Martínez-Huerta et al. 2004) even if their concentration throughout the rock is very low, as is the case in the studied vanadate-bearing emerald-green layer, at Praborna, where the bulk Σ*REE*+Y is below 8 µg/g (Table 3 in Tumiati et al. 2015, sample 18/03). In addition, the presence of halogens in retrograde metamorphic fluids, as suggested in particular by the non-negligible fluorine content of wakefieldite (Table 4), could have enhanced the solubility of *REE* (Zhou et al. 2016), promoting their removal from epidote structure.

Implications

(a) The study of tiny 10-µm-sized crystals by combining i) WDS-electron microprobe analyses, ii) Raman spectroscopy, and iii) synchrotron X-ray micro-diffraction allowed to attribute them to wakefieldite-(Ce), with notable amounts of Ca, Y and H_2O. This result demonstrates that it is now possible to routinely identify and characterize µm-sized crystals in thin sections by in-situ cutting-edge techniques, like synchrotron X-ray microdiffraction.

(b) The wakefieldite empirical formula, close to $Ce_{0.33}Y_{0.33}Ca_{0.33}VO_4 \bullet n\ H_2O$, can be described as a solid solution of 1/3 $Ce^{3+}V^{5+}O_4$ [wakefieldite-(Ce)] + 1/3 $Y^{3+}V^{5+}O_4$ [wakefieldite-(Y)] + 1/6 $Ca_2V_2O_7$, which seems consistent with the solid solution limit in $Ce_{1-x}Ca_xVO_4$ series ($x < 0.4125$: Petit et al. 2011). These results strongly suggests the existence of a partial solid solution between the wakefieldite end-member [*REE*VO_4] and a "pintadoite" end-member [$Ca_2V_2O_7$], with compositions that can vary according to the formula [wakefieldite$_{1-y/2}$ pintadoite$_{y/2}$], with $0 < y < Y_{max}$, where Y_{max} is around 1/3 (this study) and could reach 0.4125 at ambient pressure (Petit et al. 2011). The presence in one sample of even tinier crystals of some *REE*-free Ca-vanadate, with empirical formula $(Ca_{1.72}\ Sr_{0.14})\ (V^{5+}_{1.84}\ Cr^{3+}_{0.36})\ O_7$, suggests that a solvus likely exists for compositions corresponding to $y > Y_{max}$.

(c) These microcrystals were formed under low-grade metamorphic conditions in clinopyroxene + plagioclase symplectites that replaced eclogite-facies omphacite. Wakefieldite is a by-product of the breakdown of omphacite, which contains traces of vanadium, whereas some epidote, acting as a minor reactant, has provided the *REE* needed. While the omphacite contains traces of V^{3+} in the form of the natalyite end-member ($NaV^{3+}Si_2O_6$), the wakefieldite contains V^{5+}, which means that vanadium was oxidized from V^{3+} to V^{5+} during the wakefieldite formation. Thermodynamic modeling indicates that wakefieldite and other V^{5+}-bearing phases are stable where the host mineral assemblages can buffer the oxygen fugacity (i.e., the oxygen chemical potential) to extremely high

values (ΔFMQ $\geq$ +16 log units), at low- to medium-grade metamorphic conditions. This occurs in the Mn-oxide deposit of Praborna, where Mn is highly oxidized to Mn^{3+} (assemblage braunite + piemontite). We can thus expect that wakefieldite may also be found in other very oxidizing contexts.

(d) Wakefieldite and other V^{5+}-bearing minerals could be effective scavengers of *REE* in a variety of geological environments, from sedimentary to metamorphic settings, where oxidizing conditions prevail. However, the geological records of these accessory minerals are scarce, probably because they can easily go unnoticed, due to the often-small size of their crystals and their resemblance to other more common phases at the optical microscope, like the *REE* phosphates monazite (*REE*PO_4) and xenotime (YPO_4).

Acknowledgements

M. Fialin at an early stage of the study and A. Risplendente are acknowledged for their help at the electron microprobes of Paris and Milan, respectively. E. Perseil is thanked for donating sample SM96-2 to ST. Funds: Italian Ministry of Education, Universities and Research (MIUR) - Excellent Departments Project. The authors are indebted to two anonymous reviewers for their useful suggestions. Suggestions by the Associate Editor Jennifer Kung also contributed to a significant improvement of the paper.

References cited

Angiboust, S., Agard, P., Jolivet, L., and Beyssac, O. (2009) The Zermatt-Saas ophiolite: the largest (60-km wide) and deepest (*c.* 70-80 km) continuous slice of oceanic lithosphere detached from a subduction zone? Terra Nova, 21, 171–180.

Baudracco-Gritti, C., Quartieri, S., Vezzalini, G., Permingeat, F., Pillard, F., and Rinaldi, R. (1987) A lead-free wakefieldite-(Ce): New data on the mineral species corresponding to cerium orthovanadate. Bulletin de Minéralogie, 110, 657–663.

Binks, W. (1926) The crystalline structure of zircon. Mineralogical Magazine and Journal of the Mineralogical Society, 21, 176–187.

Brugger, J., Gieré, R., Graeser, S., and Meisser, N. (1997) The crystal chemistry of roméite. Contributions to Mineralogy and Petrology, 127, 136–146.

Cadoni, M., Ciriotti, M.E., and Ferraris, G. (2011) Wakefieldite-(Y) from Montaldo di Mondovì (Italy): new data and crystal structure. Rendiconti Lincei Scienze Fisiche e Naturali, 22, 307–314.

509 Cenki-Tok, B., Ragu, A., Armbruster, T., Chopin, C., and Medenbach, O. (2006) New Mn- and
510 rare-earth-rich epidote-group minerals in metacherts: manganiandrosite-(Ce) and
511 vanadoandrosite-(Ce). European Journal of Mineralogy, 18, 569–582.
512 Chang, M., Wang, M., Chen, Y., Shu, M., Zhao, Y., Ding, B., Hou, Z., and Lin, J. (2019) Self-
513 assembled $CeVO_4$/Ag nanohybrid as photoconversion agents with enhanced solar-driven
514 photocatalysis and NIR-responsive photothermal/photodynamic synergistic therapy
515 performance. Nanoscale, 11, 10129–10136.
516 Connolly, J.A.D. (2005) Computation of phase equilibria by linear programming: A tool for
517 geodynamic modeling and its application to subduction zone decarbonation. Earth and
518 Planetary Science Letters, 236, 524–541.
519 Deliens, M., and Piret, P. (1977) La kusuïte $(Ce^{3+},Pb^{2+},Pb^{4+})VO_4$, nouveau mineral. Bulletin de la
520 Société Française de Minéralogie et de Cristallographie, 100, 39–41.
521 Dubrovinsky, L., Boffa-Ballaran, T., Glazyrin, K., Kurnosov, A., Frost, D., Merlini, M., Hanfland,
522 M., Prakapenka, V.B., Schouwink, P., Pippinger, T., and others (2010) Single-crystal X-ray
523 diffraction at megabar pressures and temperatures of thousands of degrees. High Pressure
524 Research, 30, 620–633.
525 Frost, R.L., Henry, D.A., Weier, M.L., and Martens, W. (2006) Raman spectroscopy of three
526 polymorphs of $BiVO_4$: Clinobisvanite, dreyerite and pucherite, with comparisons to $(VO_4)^{3-}$
527 bearing minerals: namibite, pottsite and schumacherite. Journal of Raman Spectroscopy, 37,
528 722–732.
529 Godard, G. (2009) Two orogenic cycles recorded in eclogite-facies gneiss from the Southern
530 Armorican Massif (France). European Journal of Mineralogy, 21, 1173–1190.
531 Gröbner, J., Kolitsch, U., and Wesiger, J. (2011) New finds of vanadate and rare-earth minerals
532 from the manganese mine Ilfeld, Harz. Mineralien-Welt, 22, 41–49.
533 Harlow, G.E., and Brown, G.E.J. (1980) Low albite: an X-ray and neutron diffraction study.
534 American Mineralogist, 65, 986–995.
535 Hess, F.L. (1925) New and known minerals from the Utah-Colorado carnotite region. U.S.
536 Geological Survey Bulletin, 750, 63–78.
537 Hess, F.L., and Schaller, W.T. (1914) Pintadoite and uvanite, two new vanadium minerals from
538 Utah, a preliminary note. Journal of the Washington Academy of Sciences, 4, 576–579.
539 Holland, T., and Powell, R. (1996) Thermodynamics of order-disorder in minerals: I. Symmetric
540 formalism applied to minerals of fixed composition. American Mineralogist, 81, 1413–1424.
541 Holland, T.J.B. (1980) The reaction albite = jadeite + quartz determined experimentally in the range
542 600-1200°C. American Mineralogist, 65, 129–134.

543 Holland, T.J.B., and Powell, R. (1998) An internally consistent thermodynamic data set for phases
544 of petrological interest. Journal of Metamorphic Geology, 16, 309–343.
545 Howard, D.G., Tschernich, R.W., and Klein, G.L. (1995) Occurrence of wakefieldite-(Ce) with
546 zeolites at Yellow Lake, British Columbia, Canada. Neues Jahrbuch für Geologie und
547 Mineralogie - Monatshefte, 1995, 127–132.
548 Kim, M., Kang, Y., Cha, W., and Lee, H. (2012) Phase equilibria in the Mn–V–O system near
549 $MnO–V_2O_3$ isopleth. Journal of the American Ceramic Society, 95, 2059–2064.
550 Lavina, B., Carbonin, S., Russo, U., and Tumiati, S. (2006) The crystal structure of dissakisite-(La)
551 and structural variations after annealing of radiation damage. American Mineralogist, 91, 104–
552 110.
553 Manjón, F.J., Rodríguez-Hernández, P., Muñoz, A., Romero, A.H., Errandonea, D., and Syassen, K.
554 (2010) Lattice dynamics of YVO4 at high pressures. Physical Review B - Condensed Matter
555 and Materials Physics, 81, 1–11.
556 Martin, S., Rebay, G., Kienast, J.R., and Mével, C. (2008) An eclogitised oceanic palaeo-
557 hydrothermal field from the St. Marcel Valley (Italian Western Alps). Ofioliti, 33, 49–63.
558 Martínez-Huerta, M.V., Coronado, J.M., Fernández-García, M., Iglesias-Juez, A., Deo, G., Fierro,
559 J.L.G., and Bañares, M.A. (2004) Nature of the vanadia-ceria interface in V^{5+}/CeO_2 catalysts
560 and its relevance for the solid-state reaction toward $CeVO_4$ and catalytic properties. Journal of
561 Catalysis, 225, 240–248.
562 Merlini, M., Hanfland, M., and Crichton, W.A. (2012) $CaCO_3$-III and $CaCO_3$-VI, high-pressure
563 polymorphs of calcite: Possible host structures for carbon in the Earth's mantle. Earth and
564 Planetary Science Letters, 333–334, 265–271.
565 Miles, N.M., Hogarth, D.D., and Russell, D.S. (1971) Wakefieldite, yttrium vanadate, a new
566 mineral from Quebec. American Mineralogist, 395–410.
567 Moriyama, T., Miyawaki, R., Yokoyama, K., Matsubara, S., Hirano, H., Murakami, H., and
568 Watanabe, Y. (2011) Wakefieldite-(Nd), a New Neodymium Vanadate Mineral in the Arase
569 Stratiform Ferromanganese Deposit, Kochi Prefecture, Japan. Resource Geology, 61, 101–110.
570 O'Connor, J.R. (1966) Unusual crystal-field energy levels and efficient laser properties of
571 YVO4:Nd. Applied Physics Letters, 9, 407–409.
572 Oszlányi, G., and Sütő, A. (2004) *Ab initio* structure solution by charge flipping. Acta
573 Crystallographica Section A Foundations of Crystallography, 60, 134–141.
574 Palatinus, L., and Chapuis, G. (2007) *SUPERFLIP* – a computer program for the solution of crystal
575 structures by charge flipping in arbitrary dimensions. Journal of Applied Crystallography, 40,
576 786–790.

Panchal, V., López-Moreno, S., Santamaría-Pérez, D., Errandonea, D., Manjón, F.J., Rodríguez-Hernandez, P., Muñoz, A., Achary, S.N., and Tyagi, A.K. (2011) Zircon to monazite phase transition in CeVO4: X-ray diffraction and Raman-scattering measurements. Physical Review B - Condensed Matter and Materials Physics, 84, 1–12.

Petit, C.T.G., Lan, R., Cowin, P.I., Kraft, A., and Tao, S. (2011) Structure, conductivity and redox stability of solid solution Ce_{1-x} Ca_x VO_4 ($0 \leq x \leq 0.4125$). Journal of Materials Science, 46, 316–326.

Petříček, V., Dušek, M., and Palatinus, L. (2014) Crystallographic Computing System JANA2006: General features. Zeitschrift für Kristallographie - Crystalline Materials, 229, 345–352.

Robinson, K., Gibbs, G.V., and Ribbe, P.H. (1971) The structure of zircon: A comparison with garnet. American Mineralogist, 56, 782–790.

Ryu, M.K., Choi, J.G., Kim, G.H., Kojima, S., Takashige, M., and Jang, M.S. (2006) Raman Scattering Study in $Ca_3V_2O_8$. Ferroelectrics, 332, 1–5.

Sharma, A., Varshney, M., Chae, K.H., and Won, S.O. (2018) Electronic structure and luminescence assets in white-light emitting $Ca_2V_2O_7$, $Sr_2V_2O_7$ and $Ba_2V_2O_7$ pyro-vanadates: X-ray absorption spectroscopy investigations. RSC Advances, 8, 26423–26431.

Toffolo, L., Nimis, P., Martin, S., Tumiati, S., and Bach, W. (2017) The Cogne magnetite deposit (Western Alps , Italy): A Late Jurassic seafloor ultramafic-hosted hydrothermal system ? Ore Geology Reviews, 83, 103–126.

Tumiati, S., and Malaspina, N. (2019) Redox processes and the role of carbon-bearing volatiles from the slab–mantle interface to the mantle wedge. Journal of the Geological Society, 176, 388–397.

Tumiati, S., Godard, G., Martin, S., Nimis, P., Mair, V., and Boyer, B. (2005) Dissakisite-(La) from the Ulten zone peridotite (Italian Eastern Alps): A new end-member of the epidote group. American Mineralogist, 90, 1177–1185.

Tumiati, S., Martin, S., and Godard, G. (2010) Hydrothermal origin of manganese in the high-pressure ophiolite metasediments of Praborna ore deposit (Aosta Valley, Western Alps). European Journal of Mineralogy, 22, 577–594.

Tumiati, S., Godard, G., Martin, S., Malaspina, N., and Poli, S. (2015) Ultra-oxidized rocks in subduction mélanges? Decoupling between oxygen fugacity and oxygen availability in a Mn-rich metasomatic environment. Lithos, 226, 116–130.

Walter, V.F., Auer, C., Bojar, H., Friebe, G., Jakely, D., Kolitsch, U., Kiseljak, R., Knobloch, G., Lóránth, C., Löffler, E., and others (2018) Neue Mineralfunde aus Österreich LXVII. Carinthia II, 208, 185–254.

Weast, R.C. (1984) CRC handbook of chemistry and physics. CRC Press, USA.

Whitney, D.L., and Evans, B.W. (2010) Abbreviations for names of rock-forming minerals. American Mineralogist, 95, 185–187.

Witzke, T., Kolitsch, U., Warnsloh, J.M., and Göske, J. (2008) Wakefieldite-(La), $LaVO_4$ a new mineral species from the Glücksstern Mine, Friedrichroda, Thuringia, Germany. European Journal of Mineralogy, 20, 1135–1139.

Yu, P., and O'Keefe, T.J. (2006) The phase stability of cerium species in aqueous systems. Journal of the Electrochemical Society, 153, C80.

Zhou, L., Mavrogenes, J., Spandler, C., and Li, H. (2016) A synthetic fluid inclusion study of the solubility of monazite-(La) and xenotime-(Y) in H_2O-Na-K-Cl-F-CO_2 fluids at 800°C and 0.5 GPa. Chemical Geology, 442, 121–129.

Tables

Table 1: Electron microprobe analyses of omphacite (Omp) and symplectitic clinopyroxene (sympl Cpx) (av.=average).

Table 2: Electron microprobe analyses of other minerals in the wakefieldite-(Ce)-bearing sample SM-96-2.

Table 3: Summary features of wakefieldite minerals and selected synthetic compounds from the literature.

Table 4: Electron microprobe analyses of wakefieldite (sample SM96-2).

Figure captions

Figure 1: a) Geological sketch map of the Saint-Marcel valley and b) simplified section of the Praborna manganese-rich metacherts in contact with metabasites (bottom) and Mn-poor micaschists (top) (modified from Tumiati et al. 2015). Wakefieldite-(Ce) has been found in an emerald-green level consisting of vanadium-bearing omphacite + quartz (main accessory minerals: braunite and *REE*-bearing epidote), located in the highly oxidized basal part and showing a peculiar Mn-poor and Cr-rich bulk composition.

Figure 2: Back-scattered electron and X-ray element maps of vanadium-bearing omphacite, delimited by dashed line, surrounded by retrograde symplectites consisting of Jd-poor clinopyroxene and albitic plagioclase (sample 26/03). The white box represents the area where X-ray element maps have been collected (elements indicated in the top-left corner of each image; BSE: back-scattered image). The tiny (*REE*, Ca)-vanadates occurring in symplectites

are shown by arrows in the vanadium X-ray map. The combined map in false colors (bottom right), generated by image analysis, highlights the distribution of minerals (legend at the bottom of the figure) and shows that symplectites contain also minor phlogopite and K-feldspar. Rutile and apatite are present as accessory minerals.

Figure 3: Back-scattered electron image of wakefieldite crystals occurring in clinopyroxene + plagioclase + hematite retrograde symplectites after primary omphacite (sample SM96-2). The white box in (a) represent the area where X-ray element maps have been collected, shown in Fig. 4. Epidote and braunite (Table 2) are peak eclogite-facies minerals involved in the wakefieldite petrogenesis (see text for details).

Figure 4: Detail of Fig. 3 a, showing X-ray mapping of the wakefieldite crystal. Elements are indicated in the top-left corner of each image. The bottom-right image is an RGB combination of Y, La and Ce maps (red channel = Y; green channel = La; blue channel = Ce), highlighting the Y–(Ce+La) zonation in wakefieldite.

Figure 5: a) Raman spectrum (100–1000 cm^{-1}; 532 nm; 28 mW estimated on sample) of wakefieldite (center of the crystal in Figs. 3 a and 4), compared with two wakefieldite-(Ce) spectra available in the RRUFF database; b) the same Raman spectrum in the 3000–4000 cm^{-1} range showing bands ascribable to water of hydration and/or OH^-.

Figure 6: a) *P–T* pseudosection (isochemical diagram) calculated by thermodynamic modeling for the fixed bulk composition Na_2O = 0.709; MgO = 0.423; Al_2O_3 = 0.655; CaO = 0.832; FeO = 0.698; MnO = 1.60 (molar amounts), representing the model composition of the wakefieldite-bearing symplectite as derived from mass-balance calculations (Eq. 1), doped with 10 mol% braunite and 10% mol piemontite. Excess quartz + water and log (fO_2/1 bar) = –5.5 corresponding to ΔFMQ = +13 at P = 2.1 GPa and T = 550°C have been assumed for the calculations, in agreement with the occurrence of quartz and epidote at metamorphic peak conditions (black star; see Tumiati et al. 2015). The calculated mineral mode (vol%) at these conditions is: Omp 80.6, Grt 9.8, braunite 12.0 and Pmt 2.5. The assemblage plagioclase + jadeite-poor clinopyroxene (dashed lines: isopleths of jadeite molar fraction *Jd-in-Cpx*) occurs below the omphacite stability field; b) univariant curves in the systems V–O and Mn–V–O showing the stability field of $V^{5+}{}_2O_5$, indicative of the stability of wakefieldite. Grey field: symplectitic clinopyroxene characterized by Jd-in-Cpx = 0.06–0.13 (Table 1). The upper boundary of the stability of symplectites is represented by the "plagioclase-out" curve. Red field: subset of the grey field where V_2O_5 and hematite are both stable at log (fO_2/1 bar) = –5.5. Yellow star: preferred retrograde *P–T* estimate of wakefieldite conditions of formation at Praborna. At this conditions, the calculated mineral mode (vol%) is: Cpx 44.4, Pl 32.0,

679 braunite 13.4 Pmt 9.8 and Hem 0.4.

This is a preprint, the final version is subject to change, of the American Mineralogist (MSA)
Cite as Authors (Year) Title. American Mineralogist, in press.
DOI: https://doi.org/10.2138/am-2020-7219

Table 1: Electron microprobe analyses of omphacite (Omp) and symplectitic clinopyroxene (sympl Cpx)

	SM96-2			26/03		
oxides wt%	av. Omp (*n* =15)	Omp V max	av. sympl Cpx (*n* =5)	av. Omp (*n*= 276)	Omp V max	sympl Cpx
SiO_2	55.35	54.74	53.33	55.16	54.60	54.27
TiO_2	0.04	0.02	0.06	0.27	0.31	0.06
Al_2O_3	10.13	8.32	1.45	7.64	6.93	3.27
Cr_2O_3	0.04	0.03	0.38	0.09	0.15	0.00
Fe_2O_3	18.04	21.00	18.14	20.31	21.57	7.81
Mn_2O_3	0.23	0.21	0.00	0.00	0.25	0.00
V_2O_3	0.02	0.07	0.00	0.68	1.39	0.01
FeO	0.00	0.00	0.19	0.49	0.00	0.86
MnO	0.00	0.00	0.28	0.26	0.02	0.28
MgO	1.88	1.67	7.49	1.69	1.38	11.70
CaO	2.83	2.52	11.10	2.24	2.04	17.37
Na_2O	12.82	12.99	7.69	12.84	13.04	4.46
K_2O	0.01	0.00	0.05	0.01	0.00	0.01
Total	101.38	101.57	100.15	101.67	101.69	100.10
atoms per formula unit						
Si	1.980	1.973	1.985	1.993	1.982	1.978
Ti	0.001	0.001	0.002	0.007	0.008	0.002
Al	0.427	0.353	0.063	0.325	0.296	0.140
Cr	0.001	0.001	0.011	0.002	0.004	0.000
Fe^{3+}	0.486	0.570	0.508	0.552	0.589	0.214
Mn^{3+}	0.006	0.006	0.000	0.000	0.007	0.000
V	0.001	0.002	0.000	0.020	0.041	0.000
Fe^{2+}	0.000	0.000	0.006	0.015	0.000	0.026
Mn^{2+}	0.000	0.000	0.009	0.008	0.001	0.009
Mg	0.100	0.090	0.416	0.091	0.075	0.636
Ca	0.108	0.097	0.443	0.087	0.079	0.678
Na	0.889	0.908	0.555	0.899	0.918	0.315
K	0.001	0.000	0.002	0.000	0.000	0.000
Cations	4.000	4.000	4.000	4.000	4.000	4.000
O	5.997	5.985	6.000	6.000	6.000	6.000
End-members' molar fractions[a]						
$NaAlSi_2O_6$ (jadeite; Jd)	0.422	0.349	0.059	0.325	0.293	0.134
$NaFe^{3+}Si_2O_6$ (aegirine; Aeg)	0.481	0.566	0.504	0.552	0.586	0.208
$NaV^{3+}Si_2O_6$ (natalyite; Nt)	-0.005	-0.002	-0.005	0.020	0.037	0.000
$NaMn^{3+}Si_2O_6$ (namansilite; Nam)	0.001	0.002	-0.005	0.000	0.004	0.000

This is a preprint, the final version is subject to change, of the American Mineralogist (MSA)
Cite as Authors (Year) Title. American Mineralogist, in press.
DOI: https://doi.org/10.2138/am-2020-7219

$NaCr^{3+}Si_2O_6$ (kosmochlor; Kos)	-0.004	-0.003	0.006	0.002	0.001	0.000
$CaMgSi_2O_6$ (diopside; Di)	0.102	0.092	0.419	0.084	0.076	0.638
$CaFe^{2+}Si_2O_6$ (hedembergite; Hd)	0.002	0.002	0.009	0.008	0.001	0.028
$CaMn^{2+}Si_2O_6$ (johanssennite; Jhn)	0.002	0.002	0.012	0.001	0.002	0.011

a: Negative values should be considered as null values because they correspond to fictitious values given by the least-squares method.

This is a preprint, the final version is subject to change, of the American Mineralogist (MSA)
Cite as Authors (Year) Title. American Mineralogist, in press.
DOI: https://doi.org/10.2138/am-2020-7219

Table 2: Electron microprobe analyses of other minerals (sample SM96-2)

	epidote		hematite	braunite	plagioclase
oxides wt%	av. core (*n* =28)	av. rim (*n* =4)			
SiO_2	37.22	35.96	0.05	10.07	68.84
TiO_2	0.05	0.00	0.06	0.05	0.00
UO_2	0.00	0.05	0.01	0.06	0.00
Al_2O_3	21.37	18.12	0.03	0.03	19.97
Cr_2O_3	0.23	0.68	0.39	0.45	0.05
Fe_2O_3	8.16	11.70	85.24	9.74	0.00
Mn_2O_3	5.53	4.89	2.77	60.20	0.00
V_2O_3	0.00	0.00	0.00	0.00	0.00
La_2O_3	0.00	0.00	0.00	0.00	0.00
Ce_2O_3	0.10	0.01	0.00	0.00	0.00
Pr_2O_3	0.03	0.00	0.09	0.03	0.00
Nd_2O_3	0.05	0.04	0.00	0.00	0.00
FeO	0.00	0.00	0.00	0.00	0.54
MnO	1.47	1.66	0.00	8.67	0.07
MgO	0.05	0.02	0.01	0.27	0.00
CaO	21.77	20.95	0.05	2.12	0.08
SrO	0.62	0.46	0.13	0.18	0.00
Na_2O	0.00	0.00	0.00	0.00	11.21
K_2O	0.00	0.00	0.00	0.00	0.16
Total	96.65	94.55	88.82	91.88	100.92
a.p.f.u.					
Si	3.037	3.042	0.001	1.092	2.983
Ti	0.003	0.000	0.001	0.004	0.000
U	0.000	0.001	0.000	0.002	0.000
Al	2.055	1.807	0.001	0.003	1.020
Cr	0.015	0.046	0.009	0.039	0.002
Fe^{3+}	0.501	0.745	1.919	0.794	0.000
Mn^{3+}	0.343	0.315	0.063	4.967	0.000
V	0.000	0.000	0.000	0.000	0.000
La	0.000	0.000	0.000	0.000	0.000
Ce	0.003	0.000	0.000	0.000	0.000
Pr	0.001	0.000	0.001	0.001	0.000
Nd	0.002	0.001	0.000	0.000	0.000
Fe^{2+}	0.000	0.000	0.000	0.000	0.020

Mn^{2+}	0.102	0.119	0.000	0.796	0.003
Mg	0.006	0.003	0.000	0.044	0.000
Ca	1.903	1.899	0.001	0.246	0.004
Sr	0.029	0.023	0.002	0.011	0.000
Na	0.000	0.000	0.000	0.000	0.942
K	0.000	0.000	0.000	0.000	0.009
Cations	8.000	8.000	2.000	8.000	4.981
O	12.500	12.500	3.000	12.000	8.000

Table 3: Summary features of wakefieldite minerals and selected synthetic compounds from the literature.

Name	Chemical composition	Space group	*a* (Å)	*c* (Å)	*X*–O (Å)	V–O (Å)	Ref.
wakefieldite-(Ce)	$(Ce_{0.28}Ca_{0.27}Y_{0.27}Gd_{0.06}Nd_{0.06}Dy_{0.03}Sm_{0.03}La_{0.02}Th_{0.03})(V^{5+}_{0.91}Cr^{3+}_{0.07}Fe^{3+}_{0.02}As^{5+}_{0.01})O_4$	*I*4$_1$/*amd*	7.2233(12)	6.3949(18)	2.337	1.717	1
synthetic	$Ce_{0.7}Ca_{0.3}VO_4$	*I*4$_1$/*amd*	7.2483(3)	6.4129(3)	2.4401	1.6815	2
wakefieldite-(Ce)	$(Ce_{0.52}La_{0.18}Nd_{0.15}Y_{0.07}Pr_{0.05}Sm_{0.02})(V_{0.92}As_{0.08})O_4$	*I*4$_1$/*amd*	7.354(3)	6.488(4)	2.424	1.707	3
synthetic	$CeVO_4$	*I*4$_1$/*amd*	7.4004(1)	6.4983(6)	2.4839	1.7115	2
wakefieldite-(La)	$(La_{0.71}Nd_{0.15}Pr_{0.11}Sm_{0.01}Y_{0.02})VO_4$	*I*4$_1$/*amd*	7.432(1)	6.521(1)	2.456	1.713	4
wakefieldite-(Nd)	$(Nd_{0.40}La_{0.12}Ce_{0.11}Pr_{0.09}Y_{0.06}Sm_{0.06}Mn_{0.05}Gd_{0.05}Eu_{0.02}Dy_{0.02}Fe_{0.01})(V_{0.98}As_{0.02}Si_{0.01})O_4$	*I*4$_1$/*amd*	7.338(16)	6.509(19)	-	-	5
wakefieldite-(Y)	$(Y_{0.40}Nd_{0.15}Ce_{0.15}Ca_{0.15}Th_{0.15})(V_{0.92}As_{0.08})O_4$	*I*4$_1$/*amd*	7.2591	6.4255	-	-	6
wakefieldite-(Y)	not given	*I*4$_1$/*amd*	7.105(3)	6.29(1)	-	-	7
synthetic	YVO_4	*I*4$_1$/*amd*	7.1183(1)	6.2893(1)	2.3654	1.7088	8

1: This work; 2: Petit et al. 2011; 3: Baudracco-Gritti et al. 1987; 4: Witzke et al. 2008; 5: Moriyama et al. 2010; 6: Cadoni et al. 2011; 7: Miles and Hogarth 1971; 8: Chakoumakos et al. 1994.

This is a preprint, the final version is subject to change, of the American Mineralogist (MSA)
Cite as Authors (Year) Title. American Mineralogist, in press.
DOI: https://doi.org/10.2138/am-2020-7219

Table 4: Electron microprobe analyses of wakefieldite (sample SM96-2).

oxides wt%	average (*n* =47)	σ	max Ce	max Y	a.p.f.u.	average (*n* =47)	σ	max Ce	max Y
SiO_2	1.38	1.36	0.52	0.18	Si	0.057	0.050	0.023	0.008
As_2O_5	0.20	0.10	0.20	0.49	As^{5+}	0.005	0.002	0.006	0.012
P_2O_5	0.00	0.01	0.00	0.00	P	0.000	0.000	0.000	0.000
V_2O_5	32.98	1.18	31.64	34.09	V^{5+}	0.908	0.042	0.930	0.940
TiO_2	0.00	0.01	0.00	0.01	Ti	0.000	0.000	0.000	0.000
ThO_2	2.80	0.32	2.53	2.71	Th	0.027	0.003	0.026	0.026
UO_2	0.01	0.02	0.01	0.00	U	0.000	0.000	0.000	0.000
Al_2O_3	0.40	0.53	0.06	0.00	Al	0.020	0.023	0.003	0.000
Cr_2O_3	2.03	0.26	1.85	2.49	Cr	0.067	0.009	0.065	0.082
Fe_2O_3	0.55	0.18	0.22	0.52	Fe^{3+}	0.017	0.005	0.007	0.016
Mn_2O_3	0.06	0.04	0.00	0.07	Mn^{3+}	0.002	0.001	0.000	0.002
La_2O_3	1.32	1.80	5.11	0.03	La	0.020	0.027	0.084	0.000
Ce_2O_3	18.28	2.20	21.23	14.50	Ce	0.279	0.033	0.346	0.222
Pr_2O_3	0.00	0.00	0.00	0.00	Pr	0.000	0.000	0.000	0.000
Nd_2O_3	3.73	2.57	7.48	0.42	Nd	0.055	0.036	0.119	0.006
Sm_2O_3	1.87	0.71	2.30	0.91	Sm	0.027	0.009	0.035	0.013
Eu_2O_3	0.27	0.14	0.42	0.09	Eu	0.004	0.002	0.007	0.001
Gd_2O_3	4.11	0.68	3.92	3.27	Gd	0.057	0.008	0.058	0.045
Dy_2O_3	2.37	0.83	1.03	3.50	Dy	0.032	0.011	0.015	0.047
Y_2O_3	12.05	5.50	2.88	20.41	Y	0.267	0.117	0.068	0.453
CaO	6.06	0.76	7.30	4.86	Ca	0.271	0.034	0.348	0.217
MgO	0.00	0.00	0.00	0.00	Mg	0.000	0.000	0.000	0.000
SrO	0.06	0.06	0.00	0.00	Sr	0.002	0.001	0.000	0.000
Na_2O	0.15	0.23	0.05	0.03	Na	0.013	0.017	0.004	0.003
K_2O	0.02	0.02	0.05	0.02	K	0.001	0.001	0.003	0.001
F	0.30	0.18	-	-	Cations	2.073	-	2.124	2.088
Cl	0.03	0.02	-	-	O	3.979	-	4.000	4.000
Total	91.05	2.23	88.81	88.59	F	0.040	0.024	-	-
					Cl	0.002	0.001	-	-
					Ce/(REE+Y)	0.45	0.15	0.56	0.33
					Y/(REE+Y)	0.43	0.55	0.11	0.67
					Ca/(REE+Y)	0.37	0.05	0.48	0.28

This is a preprint, the final version is subject to change, of the American Mineralogist (MSA)
Cite as Authors (Year) Title. American Mineralogist, in press.
DOI: https://doi.org/10.2138/am-2020-7219

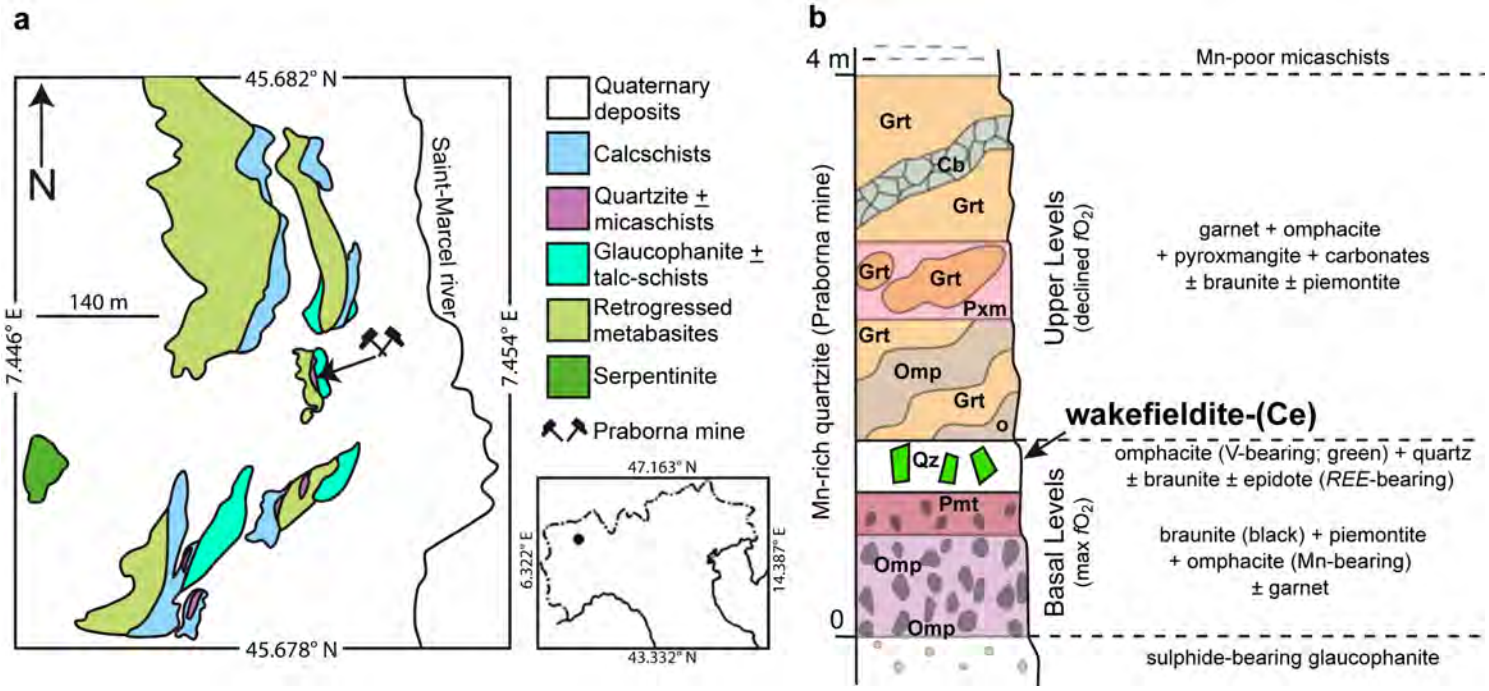

This is a preprint, the final version is subject to change, of the American Mineralogist (MSA)
Cite as Authors (Year) Title. American Mineralogist, in press.
DOI: https://doi.org/10.2138/am-2020-7219

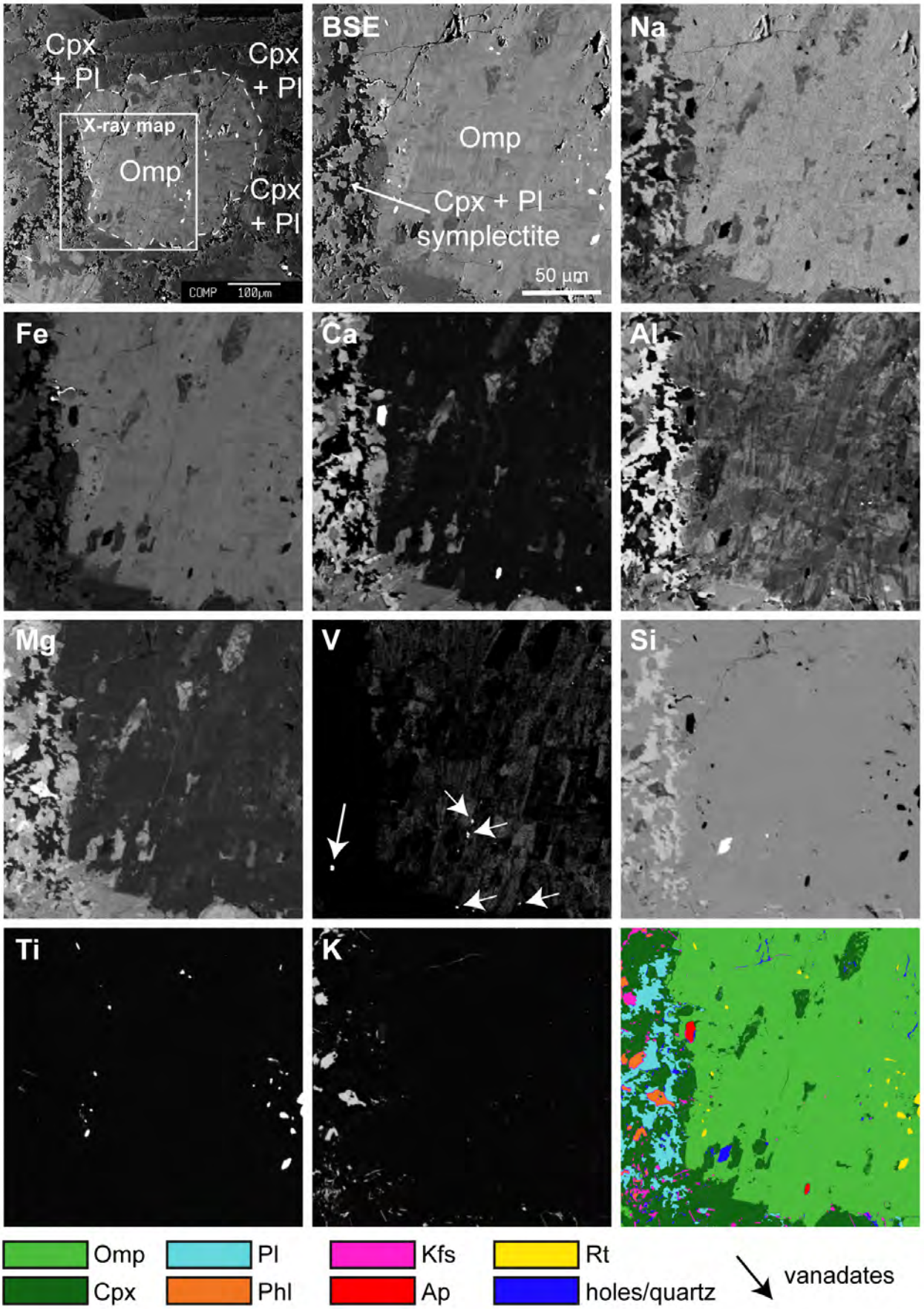

This is a preprint, the final version is subject to change, of the American Mineralogist (MSA)
Cite as Authors (Year) Title. American Mineralogist, in press.
DOI: https://doi.org/10.2138/am-2020-7219

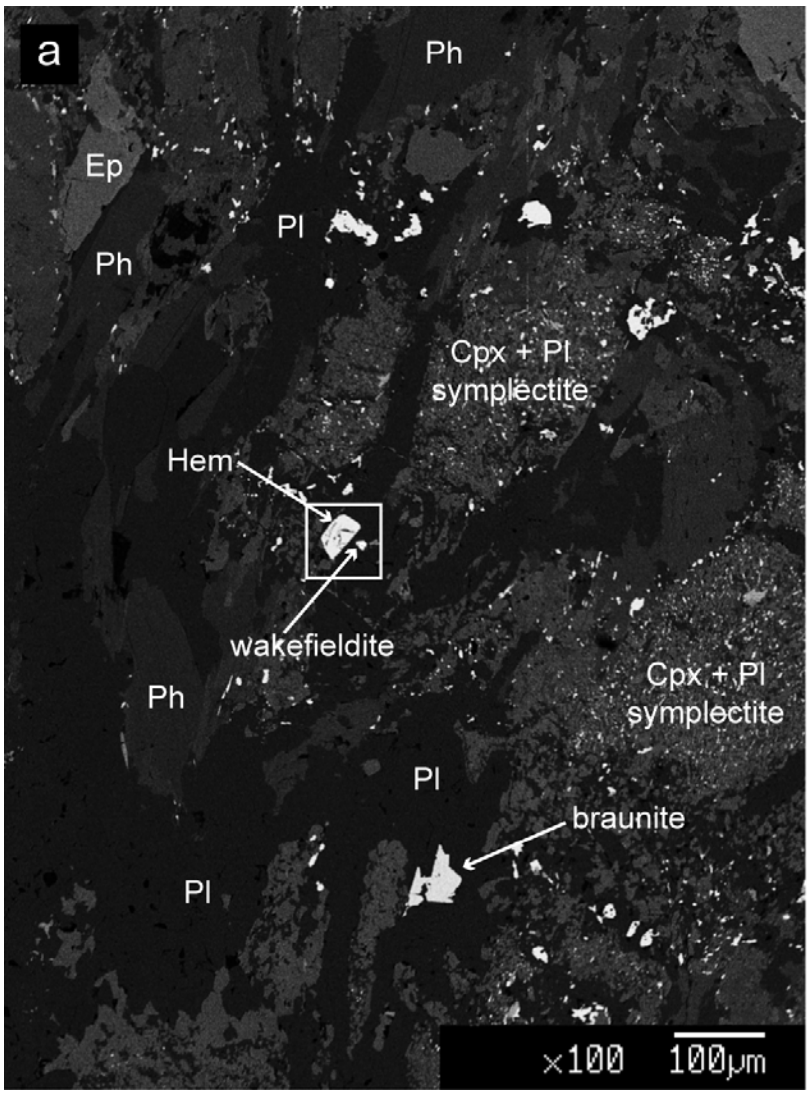

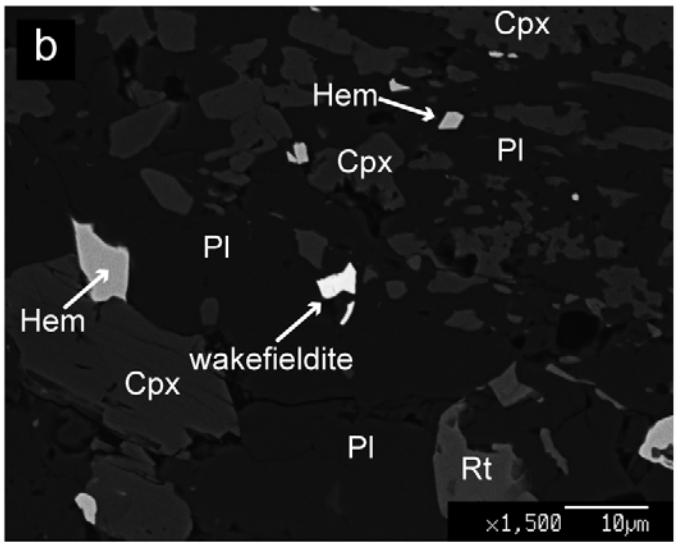

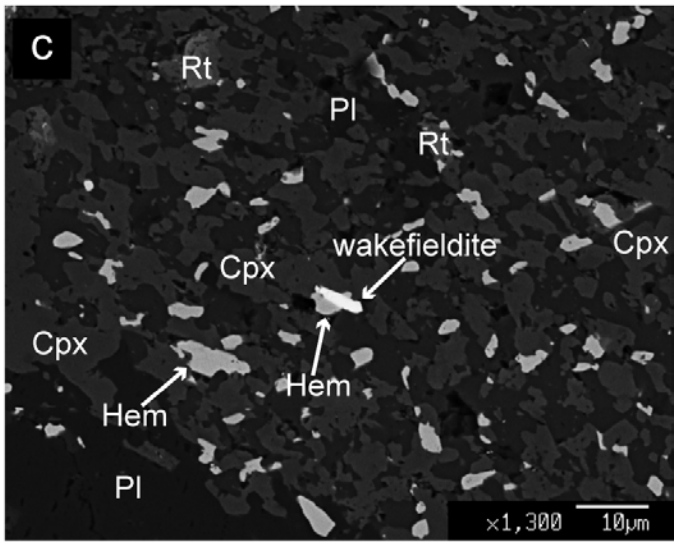

This is a preprint, the final version is subject to change, of the American Mineralogist (MSA)
Cite as Authors (Year) Title. American Mineralogist, in press.
DOI: https://doi.org/10.2138/am-2020-7219

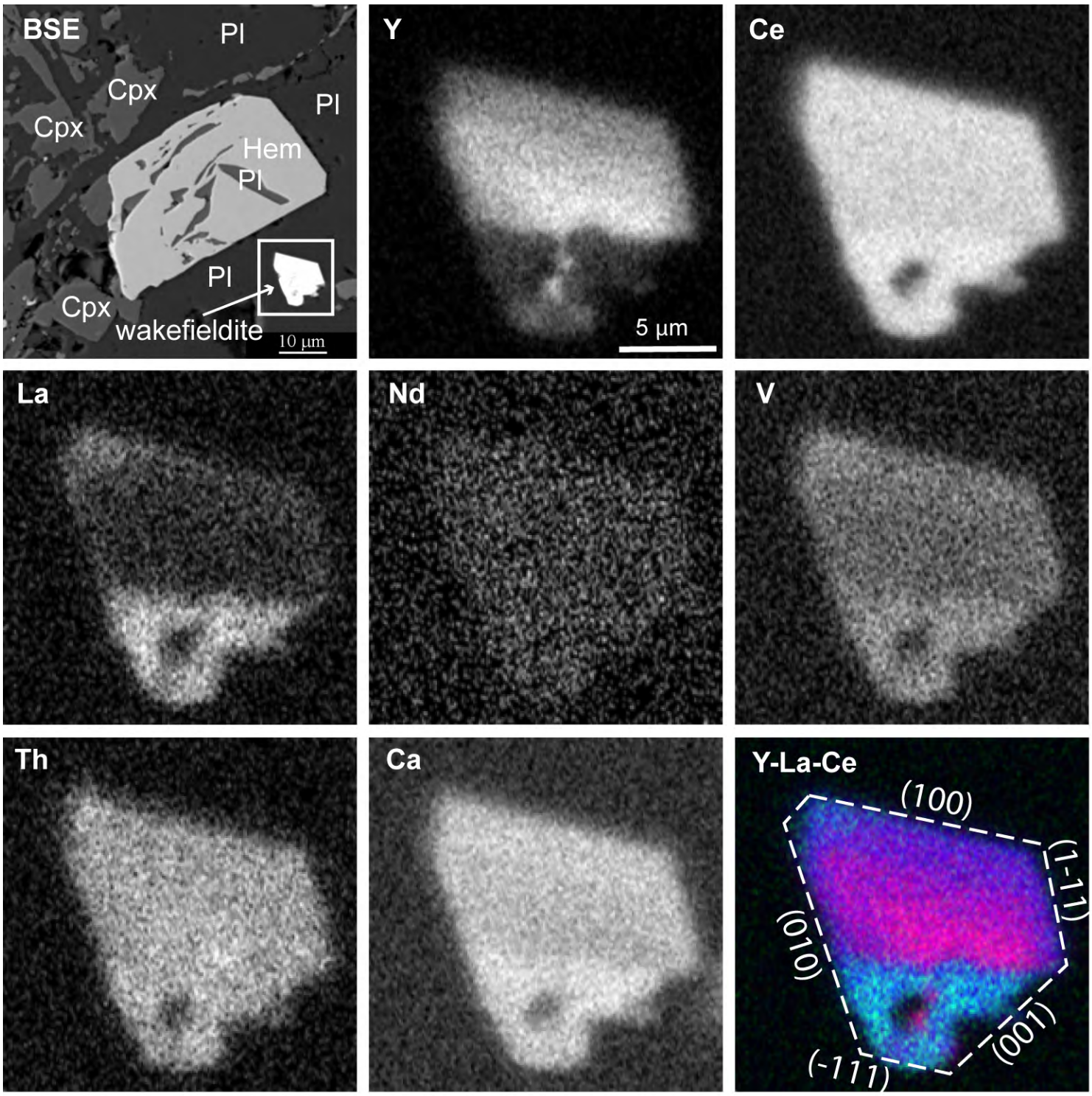

This is a preprint, the final version is subject to change, of the American Mineralogist (MSA)
Cite as Authors (Year) Title. American Mineralogist, in press.
DOI: https://doi.org/10.2138/am-2020-7219

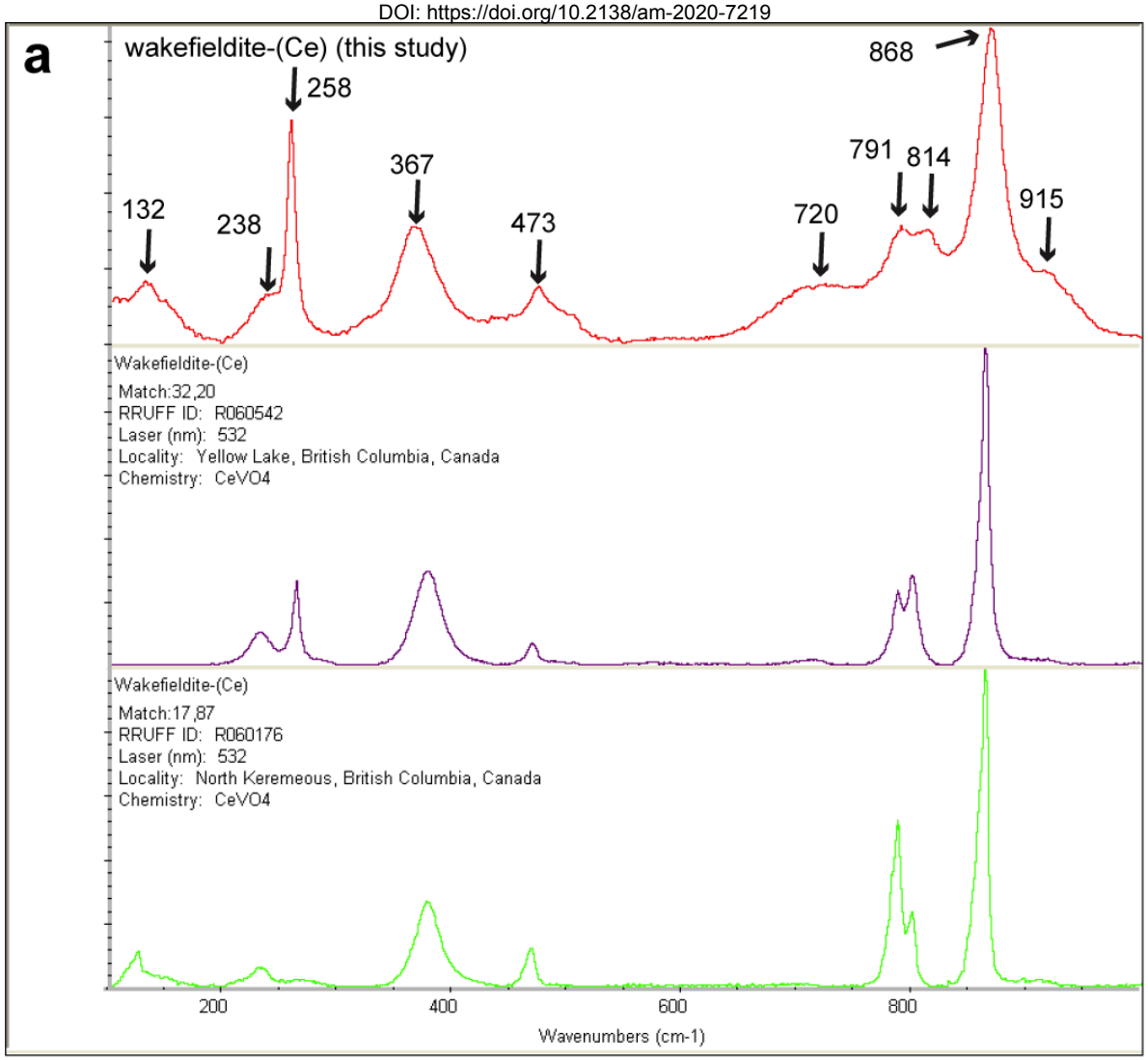

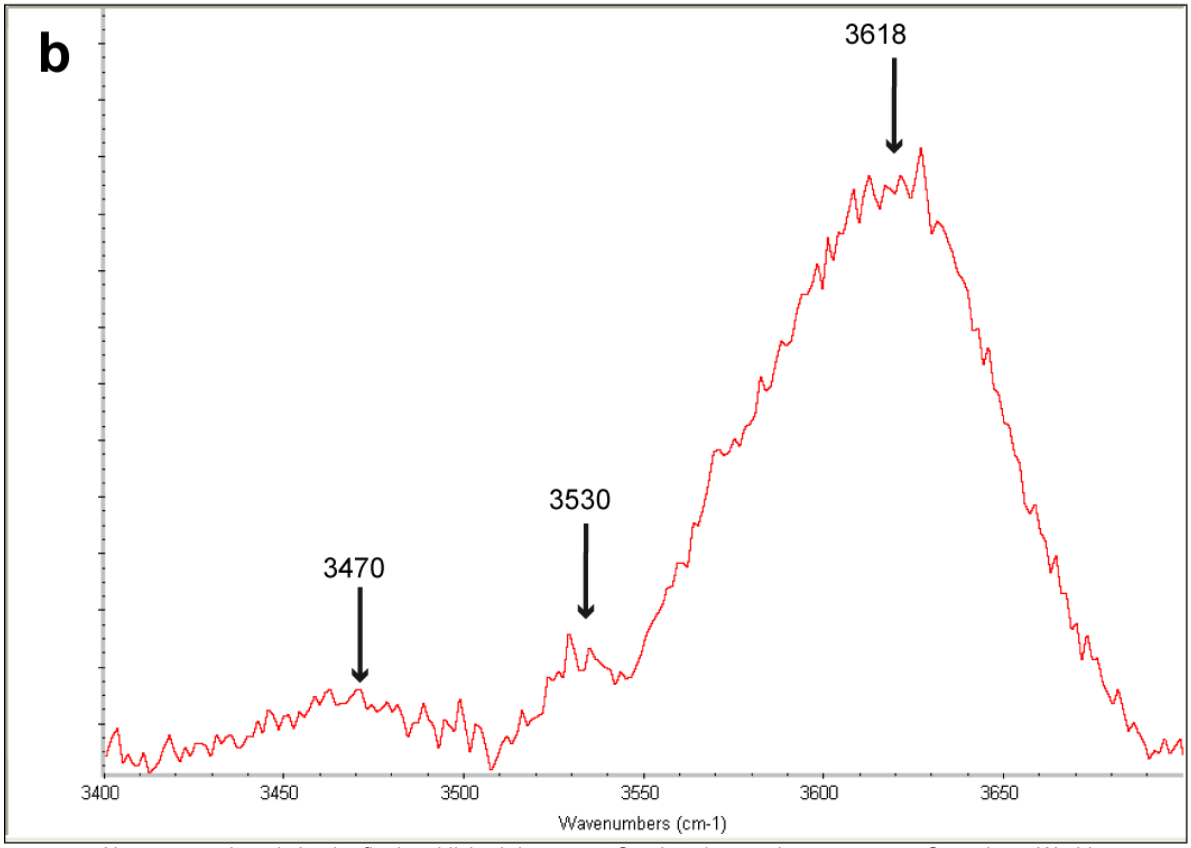

This is a preprint, the final version is subject to change, of the American Mineralogist (MSA)
Cite as Authors (Year) Title. American Mineralogist, in press.
DOI: https://doi.org/10.2138/am-2020-7219